



A novel approach for processing CaAlSiON glass-ceramics by spark plasma sintering: Mechanical and electrical properties

Sharafat Ali^{a,*}, Abbas Saeed Hakeem^b, Mirva Eriksson^c, Natalia Anna Wójcik^{a,d}

^a School of Engineering, Department of Built Environment and Energy Technology, Linnæus University, SE-351 95 Växjö, Sweden

^b Interdisciplinary Research Center for Hydrogen & Energy Storage (IRC-HES) Research Institute, King Fahd University of Petroleum & Minerals, Dhahran 31261, Saudi Arabia

^c Department of Materials and Environmental Chemistry, Stockholm University, SE-106 91 Stockholm, Sweden

^d Institute of Nanotechnology and Materials Engineering, Faculty of Applied Physics and Mathematics, Gdańsk University of Technology, Narutowicza Street 11/12, 80-233 Gdańsk, Poland

ARTICLE INFO

Keywords:

Oxynitride
Glass-ceramics
Lithium
Impedance spectroscopy
Spark plasma sintering

ABSTRACT

Lithium containing glassy materials can be used as solid electrolytes or electrode materials for lithium-ion batteries due to their high energy density. Conventional melt-quenched $\text{Ca}_{11}\text{Al}_4\text{Si}_{16}\text{O}_{49}\text{N}_{10}$ glass powder containing 24 e/o N, doped with Li-ions (1, 3, and 6 wt. %) and sintered by spark plasma sintering technique (SPS) was studied. The benefits of using SPS to produce glass-ceramics are rapid heating rates compared to conventional consolidation techniques and tuning of properties, adjusting the temperature, holding time (closed to T_g temperature), heating rate (solidification), and pressure (densification) profile during the heat treatment using SPS. Pure glass and glass-ceramic were obtained under identical SPS conditions and compared with pristine oxynitride and soda-lime-silicate (float) glasses. XRD and SEM analysis confirmed that increasing the amount of Li increases the crystallinity in the glass matrix. Nano-indentation analysis showed a decreased hardness and reduced elastic modulus values with the addition of Li-ions. The direct current conductivity increases with the addition of Li due to the high mobility of Li-ions. However, the float glass sample doped with 6 wt.% of Li exhibits even higher values of D.C. conductivity, than the analogously doped $\text{Ca}_{11}\text{Al}_4\text{Si}_{16}\text{O}_{49}\text{N}_{10}$ glass. The magnitude of activation energy (more than 1 eV) is typical for an ion hopping mechanism and the D.C. conduction mechanism is dominated by Li^+ hopping.

1. Introduction

During the last decade, there has been an increasing interest for lighter, multi-component, and hierarchically structured new oxynitride glass-ceramics having higher mechanical, thermal, and electrical properties. S.D. Stookey was the first who serendipitously discovered glass-ceramics in the middle of the last century [1]. Glass-ceramics combines the properties of glasses and ceramics by their better mechanical properties when compared to glasses and by the easiness of processing when compared to ceramics. Indeed, moulding is easier, faster, and cheaper than solid-state sintering, which is the standard way of producing crystalline ceramics [2–6]. Glass-ceramics materials exhibit favourable mechanical, electrical /electronic, magnetic properties, and chemical properties. Furthermore, substantial diversity of microstructure-property arrangements and processing routes are some

of the reasons why glass-ceramics are preferred over glasses and ceramics in many applications, e.g. optical, medical/dental, technical, electronic, architectural, and consumer. This includes the increased use of glass-ceramic materials for environmental and energy applications in the last decades.

Glass-ceramics are commonly fabricated by reheating the glass above the glass transition temperature at atmospheric pressure while nucleation and crystallisation occur. The formed glass-ceramics in turn, depend on both the composition of the base glass and the heat treatment route. In comparison with oxide-based glass-ceramics, very few studies have been conducted on oxynitride-based glass-ceramics. Furthermore, all the obtained oxynitride glass-ceramics have been prepared by the traditional heat-treatment technique [7–9]. As mentioned above, in conventional heat treatment, the parent glass is crystallized by nucleation followed by crystal growth during the stepwise heat treatment in

* Corresponding author.

E-mail addresses: sharafat.ali@lnu.se, sali@kth.se (S. Ali).

<https://doi.org/10.1016/j.jeurceramsoc.2021.09.055>

Received 13 July 2021; Received in revised form 23 September 2021; Accepted 24 September 2021

Available online 28 September 2021

0955-2219/© 2021 The Authors. Published by Elsevier Ltd. This is an open access article under the CC BY license (<http://creativecommons.org/licenses/by/4.0/>).

the furnace. This process is generally carried out at atmospheric pressure and typical heating rates vary between 5–50 °C/min, which is time-consuming. Furthermore, this limits the extent and scope of the microstructure and property optimization of these materials [8,10–13]. Here the researchers opted for a different approach for processing glass-ceramics using the spark plasma sintering (SPS) technique. The benefits of SPS are rapid heating rates compared to conventional furnaces and the possibility to apply a simultaneous uniaxial pressure and thus SPS is known for its rapid densification and is widely applied in the sintering of refractory metals and ceramics systems. SPS makes it possible to tune the properties of glass-ceramics by adjusting the temperature, holding time, heating rate, and pressure profile during the heat treatment. Moreover, another common way to modify the properties of glass-ceramics is by introducing alloying elements. The main issue in SPS processing is whether the alloying element can fully be dissolved and evenly dispersed in glass-ceramics during the fabrication process. To the best of our knowledge, there are so far no reports regarding the fabrication of oxynitride glass-ceramics by SPS technique.

In this study, the SPS technique is applied to calcium aluminosilicate oxynitride glasses (CaAlSiON). These exhibit superior mechanical, chemical, thermal, and optical properties as compared to their oxide glass counterparts [14–18]. However, the properties of CaAlSiON glasses do not solely depend on the N concentration but also the modifier element concentrations into the glass network. Compared with the bulk Ca-(Al)-Si-O-N glasses, less research has been reported on the glass-ceramics in the present system. Furthermore, there are no investigations on the effect of lithium addition on the properties of CaAlSiON glass-ceramics. However, solid ion conductors have received considerable attention, from both scientific and technological points of view, due to their low redox potential, high volumetric energy density, and atmospheric stability. In such lithium can be used in a vast variety of batteries while energy storage technologies are becoming more important in times of changing. Especially, LiAlSiO glasses and glass-ceramics nanocomposites are of considerable importance in a variety of industrial applications [19,20], and due to fast ion conducting they are considered as possible candidates for solid lithium ion batteries [21]. Therefore, the phenomenon of lithium ions diffusion in CaAlSiON system is a fascinating topic.

In this paper, the authors presented Li-doped $\text{Ca}_{11}\text{Al}_{14}\text{Si}_{16}\text{O}_{49}\text{N}_{10}$ glass-ceramic materials prepared by SPS and the impact of lithium on microstructure, density, hardness, elastic modulus, and electrical properties. This is the first paper that verifies the applicability of SPS on oxynitride glass-ceramic doped with Li ions in the CaAlSiON system.

2. Experimental procedure

Oxynitride glass with a composition of $\text{Ca}_{11}\text{Al}_{14}\text{Si}_{16}\text{O}_{49}\text{N}_{10}$ (at.%) was prepared at 1650 °C by using a radio frequency furnace. The starting powders for the parent glass were CaH_2 (95 % metal basis, Alfa Aesar GmbH & Co), Al_2O_3 (99 % ChemPur GmbH), Si_3N_4 (99 % ChemPur GmbH), SiO_2 (99.9 %, ABCR GmbH & Co). The mass of 22 g of the mixture was melted in Nb crucible in a nitrogen atmosphere. Further details concerning the glass synthesis and characterization are given in Ref. [22–26]. Li was doped to the re-ground glass matrix prior to the spark plasma sintering (SPS) (HP D5, FCT Systems, Frankenblick, Germany). 5 g of $\text{Ca}_{11}\text{Al}_{14}\text{Si}_{16}\text{O}_{49}\text{N}_{10}$ glass powder were mixed with 1, 3, and 6 wt.% of lithium where LiOH was used as a Li source. Additionally, soda-lime-silicate glass (float glass) powder (5 g) was doped with 6 wt.% of Li for comparison purposes.

Mixed powders of Li and $\text{Ca}_{11}\text{Al}_{14}\text{Si}_{16}\text{O}_{49}\text{N}_{10}$ was poured into a 20 mm diameter graphite die. A constant uniaxial pressure of 20 MPa was applied at room temperature prior to sintering at 900 °C (just below the pristine glass transition temperature, 940 °C), the used heating rate was 100 °C/min, and a soaking time of 30 min. The float glass doped with Li ions was sintered at 600 °C and uniaxial pressure of 18 MPa as powder sample melted when sintered at 750 °C. Sintering was performed in a

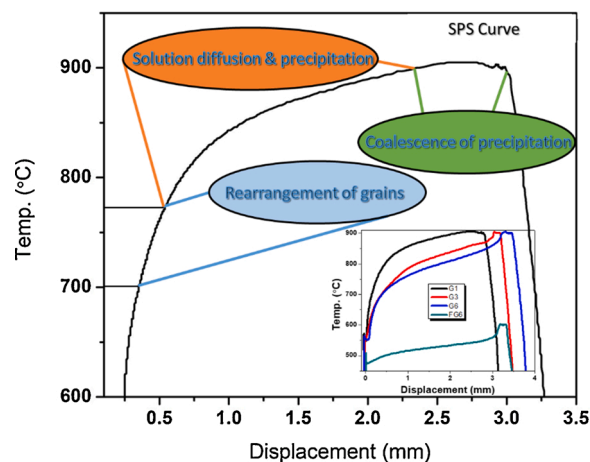


Fig. 1. Spark plasma sintering (SPS) densification curve demonstrating the sintering mechanism of sample ID G6 as an example and insert become most apparent and reveal similar behaviour for the other samples as per Table 1.

vacuum with a starting pressure of 5×10^{-2} mbar [27,28]. Fig. 1 shows SPS shrinkage curve for G6 sample and represents various stages of the sintering process of the selected sample. The trend is generally the same for all the samples (see insert Fig. 1). It is observed that fine powder particles start to rearrange themselves followed by solution-diffusion-precipitation stages that take place according to their glass transition (T_g) temperature(s). It is further observed that densification occur a bit lower than (<100 °C) the defined T_g temperature which is ascribed as the presence of the applied load during sintering of the powder mixture. Therefore, near the end of the coalescence of precipitation stage of grains, a T_g temperature expected. The attribution of the solution diffusion and precipitation stage most of the densification process accomplished. Therefore there is not much impact on the densification behaviour as the T_g temperature is similar in each composition. Additionally, on the other hand, the beginning of the final stage appeared at nearly identical temperatures for most of the glass powder samples.

Sintered glass-ceramics disks with a diameter of *c.a.* 20 mm and a thickness of around 5 mm were obtained. The graphite sheet used in the SPS process causes a contamination layer on the surface of the sintered samples. This layer was removed using SiC abrasive paper (grit sizes ranging from 120 to 1200 grit) and the final polishing for microstructure analyses was done using diamond polishing down to 1 μm finish.

Microstructure observations were carried out with an optical microscope (DSX510, Olympus, Japan) and a scanning electron microscope (JSM-7000F, JEOL, Japan with Schottky-type FEG) equipped with an energy-dispersive X-ray spectrometer (EDS detector, Oxford Instruments, UK). The SEM was operated at acceleration voltages of 15 kV, and specimen images were acquired in backscattered electron mode. X-ray diffraction (XRD) 2 θ scans were performed to determine the amorphous/crystalline nature of the pristine $\text{Ca}_{11}\text{Al}_{14}\text{Si}_{16}\text{O}_{49}\text{N}_{10}$ sample and glass-ceramics after melting and sintering SPS respectively, by using a Analytical X'pert PRO MPD diffractometer equipped with a Cu K α (1.5401 Å) source operated at 45 kV and 40 mA.

Densities were measured using Archimedes principle in deionized water ($\rho_{\text{H}_2\text{O}} = 0.998 \text{ g/cm}^3$) corrected for its temperature within 21.5 ± 0.5 °C for the measurements. A Mettler Toledo density measurement kit was used to determine the density of a solid sample. Hardness H_v and reduced elastic modulus E_r , of the glass and SPS sintered samples were measured by nano-indentation method. Nano-indentation was performed using a Nano Test Vantage instrument from Micro Materials (UK). Loading and unloading curves were produced with a standard Berkovich diamond tip at 20 mN. The Berkovich diamond tip was calibrated on a fused silica sample and 10 indentations were performed on

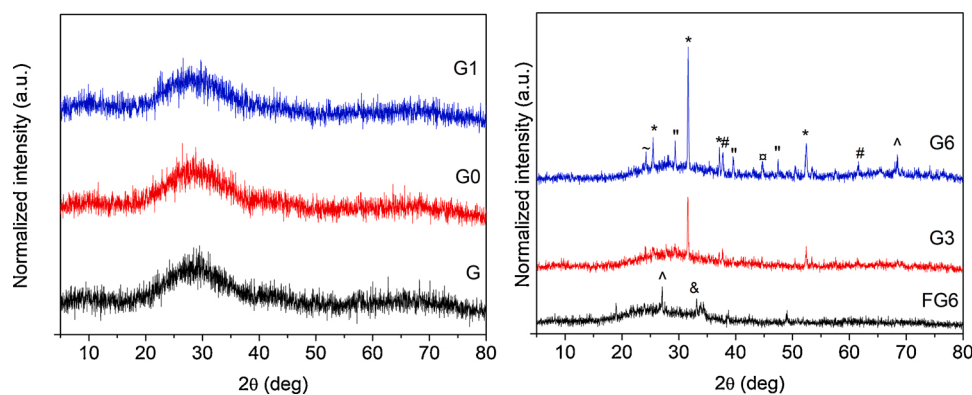


Fig. 2. X-ray diffraction patterns of samples, (left) amorphous (right) crystalline. Patterns have been offset by maximum value to allow comparison. The results of crystalline phase reflections fit and their symbols are listed in Table 2.

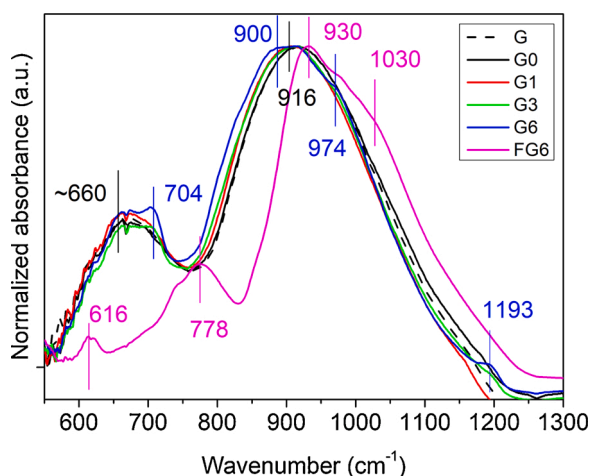


Fig. 3. FTIR spectra for all samples. All spectra are background corrected and normalized to the intensity of the high-frequency envelope at $\sim 900 \text{ cm}^{-1}$.

each sample to get a statistically valid average value. The hardness and reduced elastic modulus were calculated by the method of Oliver and Pharr using the elastic unloading part of the load-displacement curve [29]. Differential thermal analysis (DTA) measurements were performed to determine the glass/glass-ceramics transition and crystallization temperature. The measurement was made up to $1400 \text{ }^\circ\text{C}$ on powdered samples placed in Al_2O_3 crucibles and a heating rate of $20 \text{ }^\circ\text{C}/\text{min}$ under flowing nitrogen atmosphere. The instrument was used a Netzsch STA 409PC. Glass transition temperature (T_g) was estimated from the endothermic drift on the DTA curve.

Electrical measurements were conducted in the frequency range from 10 MHz to 1 MHz and the temperature range of 373 K–623 K, with an AC voltage of $1 V_{\text{rms}}$ using the Novocontrol Concept 40 broadband dielectric spectrometer. The temperature step was 10 K. The temperature was controlled using the high temperature Novotherm HT 1600 Controller. Impedance was measured on plane parallel samples in the air atmosphere. Before measurements, the sample surfaces were polished and gold electrodes were evaporated in a vacuum. The results were analysed with the use of Origin 8.5 software.

3. Results and discussion

3.1. Glass and glass-ceramics characterization

The parent oxynitride glass $\text{Ca}_{11}\text{Al}_{14}\text{Si}_{16}\text{O}_{49}\text{N}_{10}$ (at.%) prepared by melt-quenching technique is X-ray amorphous and has color opaque brown. In general, nitrogen-containing silicon base oxynitride glasses

are less transparent in the visible region due to the impurities like elemental Si and silicides present in the glass matrix. Fig. 2 displays the X-ray diffraction (left) of amorphous and partially crystalline samples (right). It can be noticed that samples G, G0, and G1 exhibit an amorphous halo typical for glasses. Samples G3, G6, and FG6 show not only the amorphous halo but their X-ray diffraction patterns also display sharp reflections of different crystalline phase(s). The intensities and broadness of the reflections change with the Li content in the glass matrix. The results of the best matching reflections fit are given in Table 2 and marked in Fig. 2. The crystallites in samples G3 and G6 (Fig. 2 (right)) are mainly various lithium silicates. However, there are also lithium aluminum silicate, lithium hydride, aluminum oxides (Al_2O_3 and $\text{Al}_{2.6}\text{O}_4$) and silicon oxide. In the following parts of this work, samples G, G0, and G1, are described as glasses, while samples G3, G6, and FG6 will be classified as glass-ceramics to underline the morphological differences between them.

Fig. 3. shows the FTIR spectra of the lithium doped $\text{Ca}_{11}\text{Al}_{14}\text{Si}_{16}\text{O}_{49}\text{N}_{10}$ glass and soda-lime-silicate glass-ceramic (sample ID FG6). All materials show mostly rounded shapes of curves bands, typical for amorphous materials. The sample FG6 shows the main bands at 930 cm^{-1} and 778 cm^{-1} , as well as two small envelopes at 1030 cm^{-1} and 616 cm^{-1} . According to the literature [30,31], the strongest high-frequency band and its small shoulder are due to Si-O band vibration (Q^2 , silicate tetrahedra with two non-bridging oxygen) and Si-O-Si stretch band, respectively. The band at 778 cm^{-1} correlates with Si-O-Si symmetric stretching vibrations of bridging oxygens between two adjacent SiO_4 tetrahedra [32]. A weak sharp shoulder observed at 616 cm^{-1} is not typical for float glass and most probably is due to the presence of silicate nanocrystallites detected by XRD [33].

In silicate glasses, the incorporation of aluminum is mainly considered to play the role of the glass former rather than the glass modifier. Especially while aluminium content is close to the one of silica as in the case of tested samples (ratio of $\text{Al}/(\text{Al} + \text{Si}) \approx 0.47$). Moreover, aluminum and silicon have similar masses and ionic ratios, favoring coupling their vibrations [34]. In that case, the presence of the Al^{3+} cations will be visible as the large downshift of the high-frequency silicate band and lower bands with increasing aluminum content [34]. FTIR spectra of the pristine glass have two prominent band envelopes in the high frequency $\sim 910 \text{ cm}^{-1}$ and low frequency $\sim 660 \text{ cm}^{-1}$ regions. The main high-frequency band is shifted into a lower frequency while compared with the one observed for sample FG6. This effect is attributed either to a gradual shift in the Si-O stretching frequency or a superposition of discrete bands due to a $\text{Si}(\text{OAl})_x$ unit, where x is the number of aluminate tetrahedra neighboring a silicate tetrahedron [31,34–36]. Moreover, the band at 665 cm^{-1} can be directly correlated with either “condensed” alumina octahedra or “isolated” alumina tetrahedra in the silicate glasses [37]. FTIR spectra of glass-ceramics G3 and G6 show also a small and sharpened peak at $\sim 704 \text{ cm}^{-1}$, which indicates the presence of AlO_6

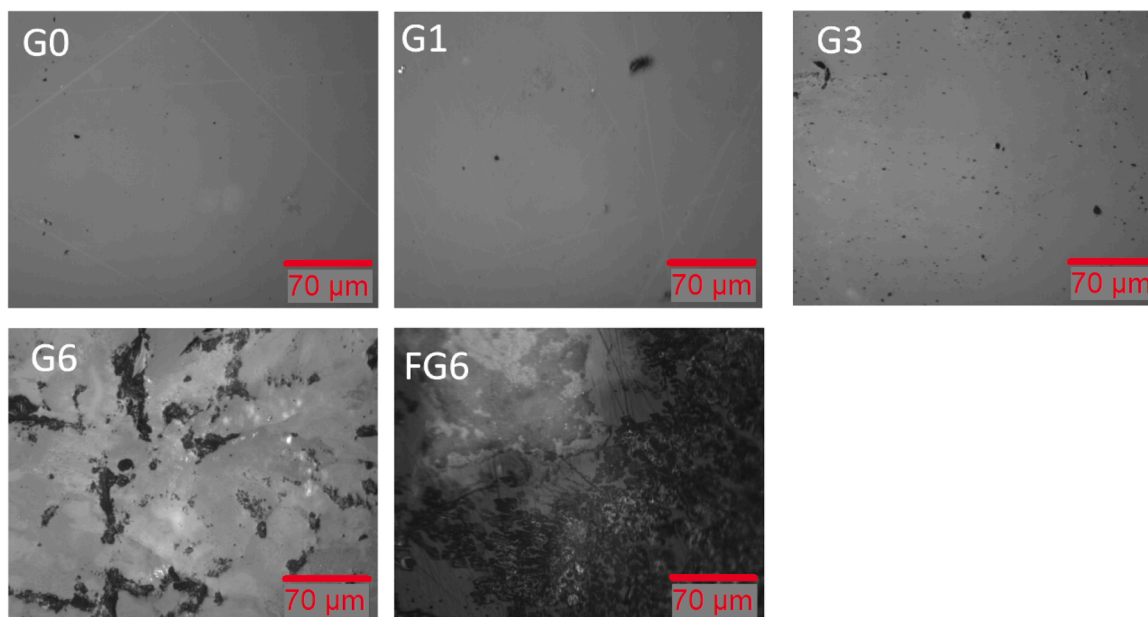


Fig. 4. Optical microscope images of the SPS sintered samples. The scale bar is 70 μm in all the micrographs.

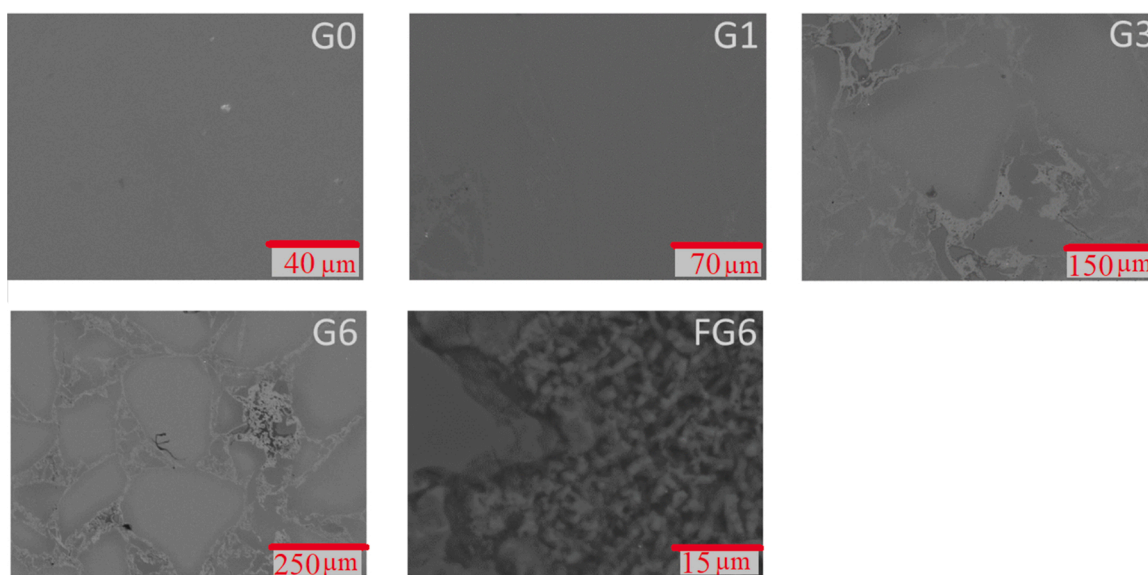


Fig. 5. SEM micrographs of $\text{Ca}_{11}\text{Al}_{14}\text{Si}_{16}\text{O}_{49}\text{N}_{10}$ and float glass after sintering in SPS.

octahedral unit in the glass structure in calcium aluminosilicate glass [38] however it can also be assigned to the silicate-aluminate nanocrystallites visible in XRD.

It is generally known that introduction of alkali cations (glass former), such as Li^+ to SiO_2 glass breaks the $\text{Si}-\text{O}-\text{Si}$ bridging bonds, creating NBOs (nonbridging oxygens). The number of NBOs increases and consequently the depolymerization of glass network following with increasing alkali ions content [32]. In tested samples, the influence of doping with Li is observed as the shift of the main band from 916 cm^{-1} into lower frequencies 900 cm^{-1} with the increase in Li content. At the same time, the additional band at 974 cm^{-1} appeared for glass-ceramic G6 doped with the highest amount of Li. This change is due to the progressive depolymerization of a silicate-aluminate network as a consequence of Li addition. The increase in Li content increases the content of silicate tetrahedral with three non-bridging oxygens (Q^1) [32]. Additionally, in two samples G3 and G6 a small and sharp shoulder is visible at $\sim 1193\text{ cm}^{-1}$ which can be correlated with Li-H vibrations

[39], what is in accordance to XRD results.

Optical microscopy observations show that the undoped glass (G0) and glass doped with 1 wt. % of Li (G1) look amorphous and homogeneous after sintering in SPS as shown in Fig. 4. Glass-ceramics (G3, G6, and FG6) show significantly different topography and contain inhomogeneities. A clear correlation between the size and amount of visible inhomogeneities and the Li content in the glass matrix can be observed. For sample G3 the inhomogeneities take the form of randomly distributed single dots, while for sample G6 they are found as bigger separated islands. The biggest inhomogeneities and connected to each other are visible for sample FG6. These observations accord with the X-ray diffraction analysis, i.e. the inhomogeneities increase with the Li content for glass samples.

SEM investigation revealed that the crystallization is most probably governed by the Li content doped in the glass matrix. Undoped sample, G0, and glass doped with 1 wt. % Li still remained glass after sintering in SPS at $900\text{ }^\circ\text{C}$ according to the X-ray diffraction analyses. These samples

Table 1

Sample designation, wt.% of Li doped, SPS sintering temperature, pressure, density (ρ), glass transition temperature (T_g), nano-hardness (H_v), and reduced elastic modulus (E_r).

| ID | Wt. % Li doped | Sintering Temp °C | Pressure MPa | ρ g/cm ³ | T_g °C | H_v GPa | E_r GPa |
|-----|----------------|-------------------|--------------|--------------------------|----------|-----------|-----------|
| G | 0 | NA | NA | 2.81 | 940 | 10.5 | 122 |
| G0 | 0 | 900 | 20 | 2.79 | 943 | 10.5 | 124 |
| G1 | 1 | 900 | 20 | 2.78 | 930 | 10.3 | 121 |
| G3 | 3 | 900 | 20 | 2.78 | NA | 10.0 | 119 |
| G6 | 6 | 900 | 20 | 2.77 | NA | 9.5 | 114 |
| FG6 | 6 | 600 | 18 | 2.48 | NA | 6.5 | 68 |

Table 2

Results of the crystalline phase reflections fit and their symbols in Fig. 2.

| Symbol | Crystalline phase |
|--------|--|
| ~ | Li ₂ Si ₃ O ₅ |
| * | Li(AlSi ₂ O ₆) |
| " | Al ₂ O ₃ |
| # | Al ₂ O ₃ |
| α | LiH |
| ^ | SiO ₂ |
| & | Li ₂ SiO ₃ |

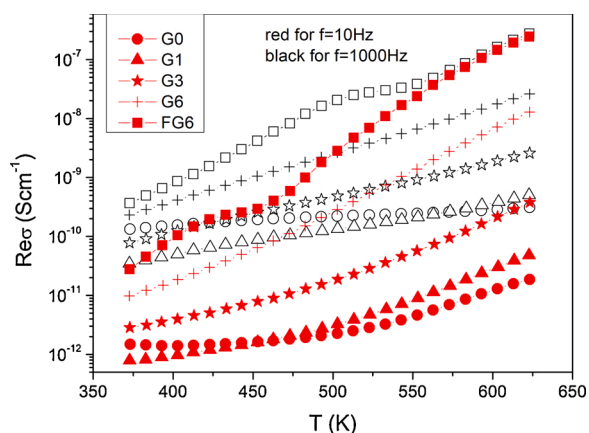


Fig. 6. The real part of A.C. conductivity as a function of temperature measured at a frequency of 10 Hz (red) and 1000 Hz (black) for all samples.

have homogenous and featureless microstructure without any visible defect or phase separation, typical for material with amorphous nature. Fig. 5. shows the microstructure of the sintered samples. It is clear that the samples G3, G6, and FG6 have crystalline microstructure.

3.2. Physical and thermal properties

The density, hardness, reduced elastic modulus, and glass transition temperature of the pristine glass and glass-ceramics are summarized in Table 1. The densities of pristine glass and the Li-doped glass-ceramic are around 2.80 g/cm³. However, no significant differences were observed between the pristine glass and the Li doped sintered glass-ceramics. The float glass-ceramic doped with 6 wt. % of Li has density values of 2.50 g/cm³, which is lower than the density of the pure float glass (2.54 g/cm³). The hardness values vary between 9.5 and 10.5 GPa and decrease with increasing the Li content in the sample. The pristine glass has slightly lower values, i.e. 10.2 GPa, than the glass-ceramic sintered without the addition of Li, i.e. 10.5 GPa. Numerous studies reveal that the hardness values decrease with the increase of modifier cations, leading to network fragmentation in silicate glass. The decrease

of hardness with the addition of Li-ion is due to the weaker M—O bonds incorporated by the Li-ions. A similar trend observed for hardness was also observed for the reduced elastic modulus, with a decrease in E_r with Li content from 124 GPa to 115 GPa, due to depolymerization of the network with the addition of Li.

Results from DTA analysis are shown in Table 1. The pristine glass (G), SPS sintered glass without Li doped (G0) and SPS sintered glass doped with 1 wt.% of Li (G1) have a glass transition temperature of 940 °C, 943 °C and 930 °C, respectively. It can be seen that the use of the SPS, did not influence the thermal properties of pristine glass. However, doping with Li decreases the T_g , which is due to the depolymerization of a silicate-aluminate network confirmed by FTIR results. The observations accord with the microscopy and X-ray analysis that the samples G, G0, and G1 are amorphous in nature. It was difficult to determine the T_g of samples, G3, G6, and FG6.

3.3. Electrical properties

The real part of alternating current (A.C.) conductivity versus temperature is displayed for all samples in Fig. 6. Red color presents the conductivity behavior measured at frequency of 10 Hz and black color for a frequency of 1000 Hz. The A.C. conductivity increase with the temperature and frequency for all tested samples, which is typical for ionic conductors [40]. The lowest values of conductivity exhibit glass G0 undoped with Li-ions and glass G1 doped only with 1 wt. % of Li. The conductivity increases with the content of Li for oxynitride samples. However, the highest values of A.C. conductivity are observed for float glass doped with 6 wt. % of Li. The highest difference in conductivity values is found for high temperatures and low frequency regions.

In Fig. 7. the A.C. conductivity is shown as a function of frequency for exemplar temperatures, for samples: (a) G0, (b) G1, (c) G3, (d) G6, and (e) FG6, respectively. The A.C. conductivity of the undoped glass, G0, (Fig. 7a) increases with the frequency in a nonlinear fashion. Below the frequency of 100 Hz the temperature effect on the conductivity parameter is visible, while at a higher frequency region, the temperature influence is unclear. Only at temperatures of 613 K and 623 K, the small frequency-independent part called direct current (D.C.) conductivity is detected. The conductivity behavior completely changed after doping with even a small amount of Li such as 1 wt. %. The A.C. conductivity spectra of all Ca₁₁Al₁₄Si₁₆O₄₉N₁₀ samples doped with Li (Fig. 7b, c, and d) can be divided into two parts: D.C. conductivity (σ_{DC}) and the A.C. conductivity (σ_{AC}), which exponentially increases with frequency. The biggest discrepancy between the conductivity of undoped glass and Li-doped samples is observed for the A.C. part. In the case of samples containing Li-ions, the σ_{AC} curves do not overlap for different temperatures. The temperature spectra separation increases with the increase in Li content. At the same time, the frequency and temperature ranges of the D.C. plateau also increase. The conductivity behavior of G1, G3 and G6 samples doped with Li can be analyzed using the Jonscher relation [41]:

$$\text{Re}\sigma(\omega) = \sigma_{DC}(T) + A(T)\omega^{s(T)} \quad (1)$$

The $\text{Re}\sigma(\omega)$ is the frequency dependence of the real part of conductivity, σ_{DC} is the frequency-independent D.C. conductivity, A is a coefficient and s is an exponent which depends on temperature and material properties. Part $A\omega^s$ describes A.C. dispersion. Additionally, in Fig. 7e, the A.C. conductivity spectra are shown for comparative sample float glass doped with 6 wt. % of Li. The conductivity curves of float glass also exhibit D.C. and A.C. conductivity parts. In the A.C. part, the additional maxima are observed. The maxima move with the temperature towards the higher frequency due to the relaxation process, which is thermally activated. This behavior is different than for A.C. part in sample G0.

The D.C. conductivity values were evaluated with the use of Jonscher power law (relation 1) from Fig. 7 and for samples G0 and FG6 by fitting

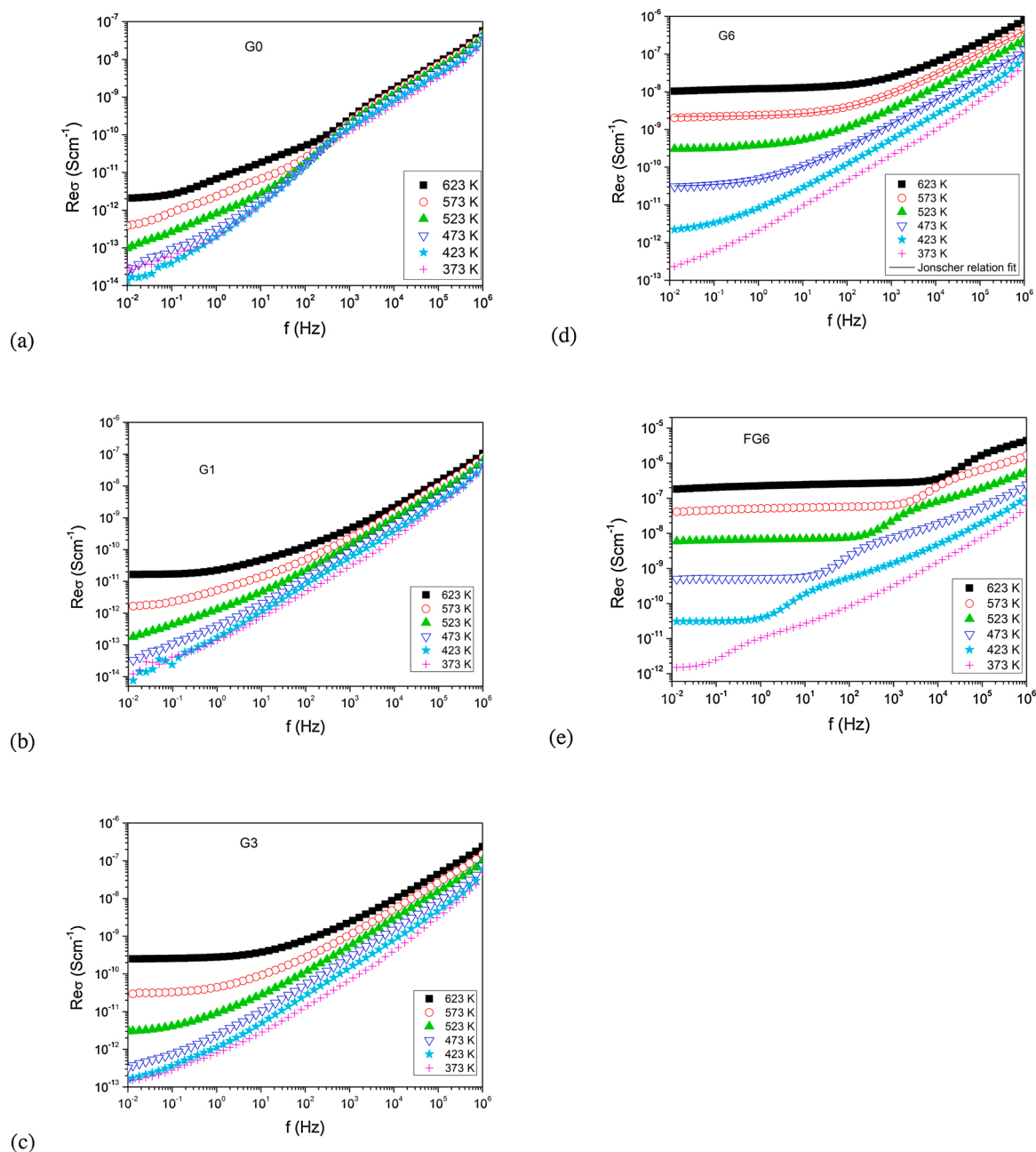


Fig. 7. The real part of A.C. conductivity as a function of frequency at different temperatures for (a) undoped glass (G0), (b) glass doped with 1 wt. % Li (G1), (c) doped with 3 wt. % Li (G3), (d) doped with 6 wt. % Li (G6), and (e) float glass doped with 6 wt. % Li (FG6).

the constant frequency-independent part. The exemplar results of fitting are shown for sample G6 in Fig. 7d. The obtained results are presented versus the reciprocal temperature for all samples in Fig. 8. The lowest values of D.C. conductivity are found for undoped glass G0. The D.C. conductivity increases after doping with Li-ions what is correlated with Li content as shown in Fig. 9a. A linear relation between D.C. conductivity of oxynitride samples and the Li content is found. The increase is 4 order of magnitude between undoped glass G0, and sample G6 doped with 6 wt. % of Li. However, comparative sample FG6 doped also with 6 wt. % of Li exhibits even higher values of D.C. conductivity, of more than one order of magnitude while comparing with analogously doped sample G6. The temperature dependences of D.C. conductivity found for all samples obey the Arrhenius law, described by the expression:

$$\sigma_{DC}T = \sigma_0 \exp\left(-\frac{E_A}{kT}\right) \quad (2)$$

Where: σ_0 is the conductivity pre-exponential factor, E_A is the activation energy for the long-range diffusion of mobile ions and k is the Boltzmann's constant. The values of E_A estimated from the fitting of Fig. 8. with Eq. (2) are listed in Fig. 8. for samples doped with Li. Additionally, the activation energy is displayed as a function of Li content in Fig. 9b. It can be seen that its value is the highest for sample G1 and it decreases with the increase in Li concentration. The magnitude of activation energy observed for all samples doped with Li-ions (more than 1 eV) is typical for an ion hopping mechanism. In all $\text{Ca}_{11}\text{Al}_{14}\text{Si}_{16}\text{O}_{49}\text{N}_{10}$ samples doped with the Li-ions, the D.C. conduction mechanism is dominated by Li^+ hopping. However, as we used LiOH as dopant, the possible second type of charge carrier: proton ions, is likely [42]. Moreover, undoped glass G0 does not contain lithium and proton ions; it also exhibits D.C. conductivity at the temperatures of 613 K and 623 K. In the case G0, we suppose that it exhibits a typical ionic conductivity with

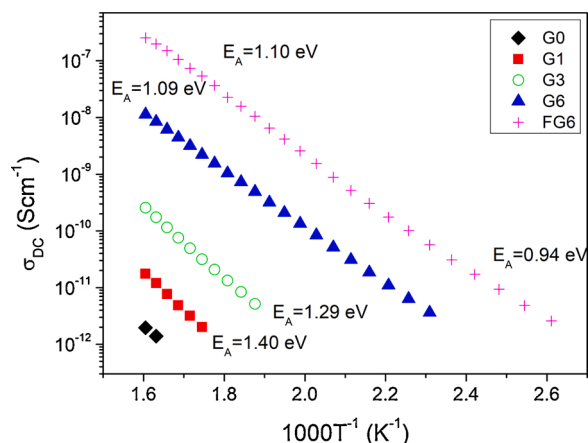


Fig. 8. The D.C. conductivity versus reciprocal conductivity for all samples.

oxygen ions as charge carriers [42]. At the same time, we suggest that this conduction mechanism may also be observed in all doped $\text{Ca}_{11}\text{Al}_{14}\text{Si}_{16}\text{O}_{49}\text{N}_{10}$ samples. Therefore, their estimated D.C. conductivity and activation energy values are a sum of all three possible charge carriers contributions. However, their clear correlation with the Li quantity unequivocally points to the domination of the Li^+ hopping mechanism (Fig. 9). The situation for competitive sample float glass

doped with 6 wt. % of Li is even more complicated as it contains ~ 13 wt. % of Na. The possible conduction mechanism in the float glass sample is due to different ions hopping: Li^+ , Na^+ , H^+ , and O^{2-} . Moreover, in float glass, the activation energy can be divided into low and high temperature regions. The highest values of D.C. conductivity and lower activation energy for low temperature range in sample FG6 can be correlated with significantly higher content of all alkali than in G6.

Fig. 10. shows the imaginary part of the impedance as a function of frequency in log-log scale for all samples measured at a temperature of 613 K. In the imaginary part, a maximum is clearly visible in all samples. The frequency position of maximum moves into the higher frequency region with the increase in Li content for all samples. However, the shape of the maximum is not symmetrical and suggests more than one relaxation process. Moreover, in the samples G3, G6, and FG6, a further increase in the imaginary part of impedance with the decrease in frequency is found. This process can be correlated with the polarization effect due to charge carriers accumulation on electrodes. In the real part of impedance behavior, the D.C. part can be observed for all samples (Fig. 10 insert). However, the transition in the A.C. region can be observed, especially in sample FG6 what is in agreement with the asymmetric shape of maximum in the imaginary part. Additionally, on the right side of Fig. 10, the Nyquist plots (the imaginary versus real part of impedance) are shown for samples G3, G6, and FG6. In all three spectra, a minimum of two semicircles can be noticed and the beginning of the third one. These semicircles can be correlated with the two or more relaxation processes,

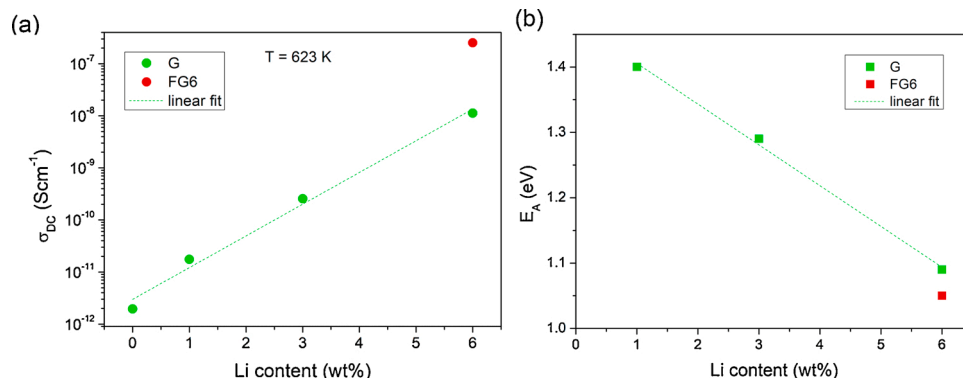


Fig. 9. (a) D.C. conductivity at 623 K and (b) activation energy versus the Li content for all samples.

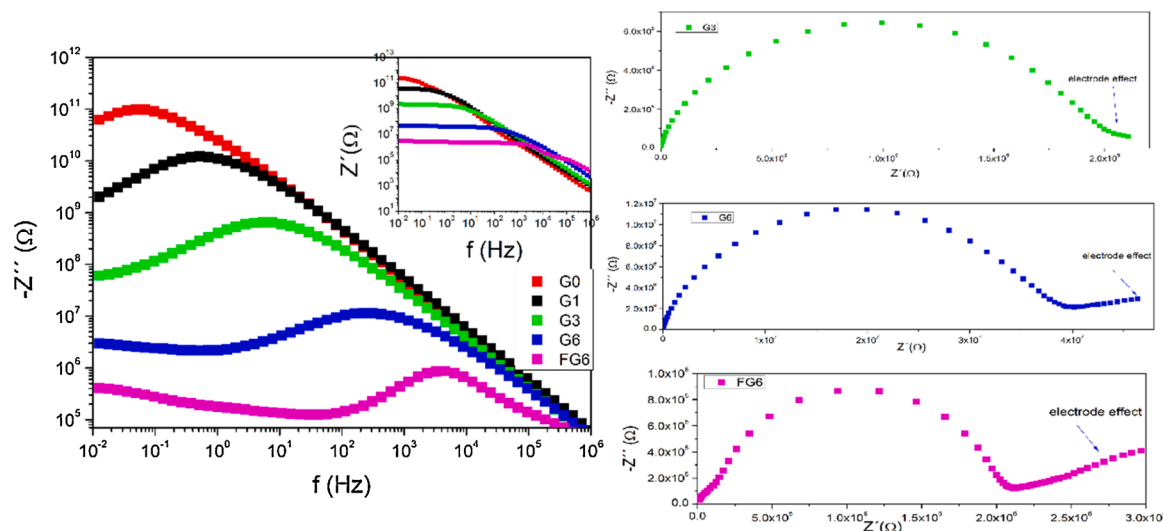


Fig. 10. Imaginary part of impedance as a function of frequency while insert presents the real part of impedance as a function of frequency both in log-log scale for samples G0, G1, G3, G6, and FG6 (left). Nyquist plots for samples G3, G6 and FG6. All results are shown for the temperature of 613 K (right).

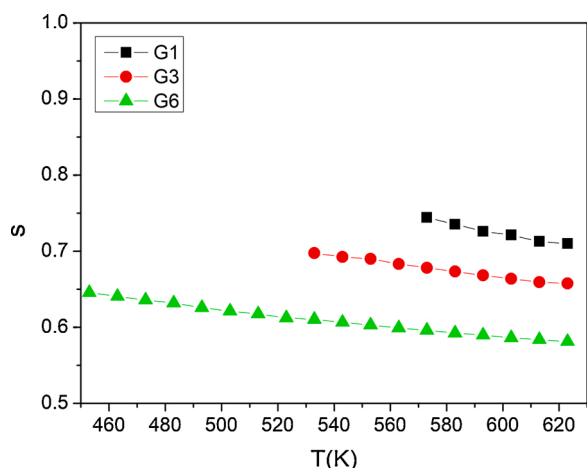


Fig. 11. Exponent s as a function of temperature for samples G1, G3 and G6.

which occurred in samples. This observation is in accord with the previous statement that the conduction mechanism in the studied samples is due to more than one kind of ion hopping. However, in the case of glass-ceramic materials, more than one relaxation process can be as well correlated with the presence of crystallites and possible grain boundaries/interface. The visible beginning of the third process can be assigned to the electrode and/or grain boundary effect [43,44].

Based on Jonscher relation (relation 1) it was possible to estimate exponent s for samples G1, G3, and G6 which did not show additional relaxation in the A.C. conductivity region. Fig. 11. displays the obtained s values as a function of temperature. The exponent s can be useful in the prediction of conduction mechanism in glasses and glass-ceramics. The value of s ranging between 0 and 1 indicates that the hopping motion involved is a translational motion with a sudden hopping [45]. However, in the ion-conductors, the parameter s mostly can be found between 0.5 and 1 and can be correlated with the ideal long range pathways and diffusion limited hopping. For samples G1, G3 and G6, the parameter s lies between 0.6 and 0.8 and slightly decreases with temperature. The lowest values of parameter s for glass G1 can be due to a low rate of successful jumps, which results in low D.C. conductivity values as compare to other samples [46]. The s values decrease with the increase in Li content for samples G3 and G6. Additionally, the temperature range in which the s could be correctly fitted also increases. Increasing the content of mobile ions, the interaction between them and the lattice around them also increases, which leads to the reduction in the value of exponent s . Therefore, these changes can be correlated with the increase in the rate of successful jumps of ions, resulting in the increased value of D.C. conductivity.

4. Conclusions

Ca containing SiAlON ceramics doped with different concentrations of Li-ions were prepared by spark plasma sintering technique. Samples sintered with ≤ 1 wt. % of Li-ions addition were amorphous after sintering in SPS at 900 °C, and 20 MPa. The crystallinity increase with increasing the content of Li-ions and the most crystalline sample consists of crystalline phases of $\text{Li}(\text{AlSi}_2\text{O}_6)$, $\text{Li}_2\text{Si}_3\text{O}_5$, and Li_2SiO_3 . The results demonstrate that tailoring the mechanical and electrical properties of oxynitride glass and glass-ceramics can be achieved by varying the Li content in the glass matrix. Like the pristine glass, the sintered samples were not transparent. The soda-lime-silicate glass doped with 6 wt. % of Li also turns to be translucent after sintering. Small variation in densities was observed for oxynitride sample doped with Li-ions, but in the case of soda-lime-silicate glass, the density decrease from 2.54 g/cm³ for pristine soda-lime-silicate glass to 2.48 g/cm³ for Li doped one. Glass transition temperature, hardness, and reduced elastic modulus values

decrease with increasing the Li content in the glass matrix for both $\text{Ca}_{11}\text{Al}_{14}\text{Si}_{16}\text{O}_{49}\text{N}_{10}$ glass-ceramics and soda-lime-silicate glass. The electrical properties of CaSiAlON glasses and glass-ceramics depend on Li doping. The D.C. conductivity increases by 4 order of magnitude and its activation energy decrease from 1.4 to 1.1 eV with the addition of 6 wt. % of Li. The conduction mechanism is dominated by Li-ions hopping in all Li-doped samples; however, also hopping of oxygen vacancies and/or protons is possible in the glasses and glass-ceramics. The conductivity variations with the Li content are due to changing the rate of successful jumps between ions. Increasing the content of mobile ions in the tested samples, the interaction between them and the lattice around them also increases, which leads to the increase in the rate of successful jumps of ions, resulting in the increased value of D.C. conductivity.

Declaration of Competing Interest

The authors report no declarations of interest.

Acknowledgements

This work was supported by the STINT (Grant No. MG 2018-7558). Abbas Saeed Hakeem acknowledge the financial support from the Deanship of Research at King Fahd University of Petroleum and Minerals (KFUPM), Dhahran, Saudi Arabia.

References

- [1] S.D. Stookey, *Method of Making Ceramics and Product Thereof*, 920, 1956, p. 971.
- [2] J. Deubener, M. Allix, M.J. Davis, A. Duran, T. Höche, T. Honma, T. Komatsu, S. Krüger, I. Mitra, R. Müller, S. Nakane, M.J. Pascual, J.W.P. Schmelzer, E. D. Zanotto, S. Zhou, Updated definition of glass-ceramics, *J. Non-Cryst. Solids* 501 (2018) 3–10.
- [3] Q. Fu, G.H. Beall, C.M. Smith, J.T. Kohli, R.E. Youngman, B.R. Wheaton, A. J. Credle, O. Gulbitten, Strong, tough glass-ceramics for emerging markets, *Int. J. Appl. Glass Sci.* 7 (2016) 486–491.
- [4] L.L. Hench, Glass and glass-ceramic technologies to transform the world, *Int. J. Appl. Glass Sci.* 2 (2011) 162–176.
- [5] M.J. Davis, E.D. Zanotto, Glass-ceramics and realization of the unobtainable: property combinations that push the envelope, *MRS Bull.* 42 (2017) 195–199.
- [6] V.O. Soares, F.C. Serbena, G.D.S. Oliveira, C. da Cruz, R.F. Muniz, E.D. Zanotto, Highly translucent nanostructured glass-ceramic, *Ceram. Int.* 47 (2021) 4707–4714.
- [7] R.R. Wusirikka, C.K. Chyung, Oxynitride glasses and glass-ceramics, *J. Non-Cryst. Solids* 38–39 (1980) 39–44.
- [8] S. Hampshire, Oxynitride glasses, their properties and crystallisation – a review, *J. Non-Cryst. Solids* 316 (2003) 64–73.
- [9] M.A. Sainz, P. Miranzo, M.I. Osendi, Sintering behaviour and properties of YAlSiO and YAlSiON glass-ceramics, *Ceram. Int.* 37 (2011) 1485–1492.
- [10] T.R. Dinger, Microstructure development during controlled crystallization of M-Si-O-N glass-ceramics, *Mater. Sci. Forum* 47 (1991) 119–131.
- [11] G.H. Liu, Z.Z. Zhou, Q.H. Wei, F. Fei, H. Yang, Q. Liu, Preparation and tunable optical properties of ion beam sputtered SiAlON thin films, *Vacuum* 101 (2014) 1–5.
- [12] R. Ramesh, E. Nestor, M.J. Pomeroy, S. Hampshire, Classical and differential thermal analysis studies of the glass-ceramic transformation in a YSiAlON glass, *J. Am. Ceram. Soc.* 81 (1998) 1285–1297.
- [13] K. Lederer, M. Deckwerth, C. Rüssel, Zirconia-doped Mg-Ca-Al-Si-O-N glasses: crystallization, *J. Non-Cryst. Solids* 224 (1998) 109–121.
- [14] A. Sharafat, J. Grins, S. Esmailzadeh, Hardness and refractive index of Ca-Si-O-N glasses, *J. Non-Cryst. Solids* 355 (2009) 301–304.
- [15] A. Sharafat, Preparation, Characterization and Properties of Nitrogen Rich Glasses in Alkaline Earth-Si-O-N Systems, Institutionen för fysikalisk kemi, oorganisk kemi och strukturkemi, Stockholm, 2009, p. 116.
- [16] S. Hampshire, A.R. Hanifi, A. Genson, M.J. Pomeroy, Ca-Si-Al-O-N glasses: effects of fluorine on glass formation and properties, *Key. Eng. Mat.* 352 (2007) 165–172.
- [17] J.E. Shelby, Formation and properties of calcium aluminosilicate glasses, *J. Am. Ceram. Soc.* 68 (1985) 155–158.
- [18] S. Sakka, K. Kamiya, T. Yoko, Preparation and properties of Ca-Al-Si-O-N oxynitride glasses, *J. Non-Cryst. Solids* 56 (1983) 147–152.
- [19] S. Ross, A.-M. Welsch, H. Behrens, Lithium conductivity in glasses of the $\text{Li}_2\text{O} - \text{Al}_2\text{O}_3 - \text{SiO}_2$ system, *Phys. Chem. Chem. Phys.* 17 (2014).
- [20] A.-M. Welsch, H. Behrens, S. Ross, D. Murawski, Structural control of ionic conductivity in $\text{LiAlSi}_2\text{O}_6$ and $\text{LiAlSi}_4\text{O}_{10}$ glasses and single crystals, *Zeitschrift für Physikalische Chemie* 226 (2012) 491.
- [21] A. Kuhn, M. Wilkening, P. Heitjans, Mechanically induced decrease of the Li conductivity in an aluminosilicate glass, *Solid State Ionics* 180 (2009) 302–307.
- [22] S. Ali, B. Jonsson, Glasses in the Ba-Si-O-N system, *J. Am. Ceram. Soc.* 94 (2011) 2912–2917.

- [23] S. Ali, B. Jonson, M.J. Pomeroy, S. Hampshire, Issues associated with the development of transparent oxynitride glasses, *Ceram. Int.* 41 (2015) 3345–3354.
- [24] A. Sharafat, J. Bo, Compositional effects on the properties of high nitrogen content alkaline-earth silicon oxynitride glasses, AE= Mg, Ca, Sr, Ba, *J. Eur. Ceram. Soc.* 31 (2011) 611–618.
- [25] A. Sharafat, B. Forslund, J. Grins, S. Esmailzadeh, Formation and properties of nitrogen-rich strontium silicon oxynitride glasses, *J. Mater. Sci.* 44 (2009) 664–670.
- [26] A. Sharafat, J. Grins, S. Esmailzadeh, Glass-forming region in the Ca–Si–O–N system using CaH₂ as Ca source, *J. Eur. Ceram. Soc.* 28 (2008) 2659–2664.
- [27] H.M. Irshad, A.S. Hakeem, B.A. Ahmed, S. Ali, S. Ali, S. Ali, M.A. Ehsan, T. Laoui, Effect of Ni content and Al₂O₃ particle size on the thermal and mechanical properties of Al₂O₃/Ni composites prepared by spark plasma sintering, *Int. J. Refract. Met. Hard Mater.* 76 (2018) 25–32.
- [28] A.S. Hakeem, M. Khan, B.A. Ahmed, A. Al Ghanim, F. Patel, M.A. Ehsan, S. Ali, T. Laoui, S. Ali, Synthesis and characterization of alkaline earth and rare earth doped sialon Ceramics by spark plasma sintering, *Int. J. Refract. Met. Hard Mater.* 97 (2021).
- [29] W.C. Oliver, G.M. Pharr, An improved technique for determining hardness and elastic-modulus using load and displacement sensing indentation experiments, *J. Mater. Res.* 7 (1992) 1564–1583.
- [30] P. McMillan, Structural studies of silicate glasses and melts-applications and limitations of Raman spectroscopy, *Am. Mineral.* 69 (1984) 622–644.
- [31] E.I. Kamitsos, J.A. Kapoutsis, H. Jain, C.H. Hsieh, Vibrational study of the role of trivalent ions in sodium trisilicate glass, *J. Non-Cryst. Solids* 171 (1994) 31–45.
- [32] T. Furukawa, K.E. Fox, W.B. White, Raman-spectroscopic investigation of the structure of silicate-glasses. 3. Raman intensities and structural units in sodium-silicate glasses, *J. Chem. Phys.* 75 (1981) 3226–3237.
- [33] Y. Huang, Z. Jiang, W. Schwieger, Vibrational spectroscopic studies of layered silicates, *Chem. Mater.* 11 (1999) 1210–1217.
- [34] S.-L. Lin, C.-S. Hwang, J.-F. Lee, Characterization of CeO₂–Al₂O₃–SiO₂ glasses by infrared and x-ray absorption near edge structure spectroscopies, *J. Mater. Res.* 11 (1996) 2641–2650.
- [35] P. McMillan, B. Piriou, A. Navrotsky, A Raman-spectroscopic study of glasses along the joins silica-calcium aluminate, silica-sodium aluminate, and silica-potassium aluminate, *Geochim. Cosmochim. Acta* 46 (1982) 2021–2037.
- [36] P. McMillan, Structural studies of silicate-glasses and melts - applications and limitations of Raman-spectroscopy, *Am. Mineral.* 69 (1984) 622–644.
- [37] P. Tarte, Infra-red spectra of inorganic aluminates and characteristic vibrational frequencies of AlO₄ tetrahedra and AlO₆ octahedra, *Spectrochim. Acta Part A: Mol. Spectrosc.* 23 (1967) 2127–2143.
- [38] C. Huang, E.C. Behrman, Structure and properties of calcium aluminosilicate glasses, *J. Non-Cryst. Solids* 128 (1991) 310–321.
- [39] X. Wang, L. Andrews, Infrared spectra of thallium hydrides in solid neon, hydrogen, and argon, *J. Phys. Chem. A* 108 (2004).
- [40] N.A. Wójcik, P. Kupracz, R.J. Barczyński, B. Jonson, S. Ali, Ion conduction in beryllium-alumino-silicate glasses doped with sodium or sodium and lithium ions, *Solid State Ionics* 341 (2019), 115055.
- [41] A.K. Jonscher, Universal dielectric response, *Nature* 267 (1977) 673–679.
- [42] J. Karczewski, T. Miruszewski, B. Bochentyn, B. Kusz, Determination of ionic conductivity in the Bi-Si-O and Pb-Si-O glasses, *Mater Sci-Poland* 35 (2017).
- [43] N.A. Szreder, P. Kupracz, M. Przeźniak-Welenc, J. Karczewski, M. Gazda, R. J. Barczyński, Nonlinear and linear impedance of bismuth vanadate ceramics and its relation to structural properties, *Solid State Ionics* 271 (2015) 86–90.
- [44] N.A. Wójcik, P. Kupracz, R.J. Barczyński, Nonlinear electrical properties of glass-ceramics nanocomposites containing ferroelectric nanocrystallites of Bi₂VO_{5.5}, *Solid State Ionics* 317 (2018) 7–14.
- [45] K. Funke, Jump relaxation in solid electrolytes, *Prog. Solid State Chem.* 22 (1993) 111–195.
- [46] S.R. Elliott, A.P. Owens, The diffusion-controlled relaxation model for ionic transport in glasses, *Philos. Mag. B* 60 (1989) 777–792.